

This is the accepted manuscript made available via CHORUS. The article has been published as:

Fast ion swapping for quantum-information processing

H. Kaufmann, T. Ruster, C. T. Schmiegelow, M. A. Luda, V. Kaushal, J. Schulz, D. von Lindenfels, F. Schmidt-Kaler, and U. G. Poschinger

Phys. Rev. A **95**, 052319 — Published 10 May 2017

DOI: [10.1103/PhysRevA.95.052319](https://doi.org/10.1103/PhysRevA.95.052319)

Fast ion swapping for quantum information processing

H. Kaufmann,¹ T. Ruster,¹ C. T. Schmiegelow,^{1,*} M. A. Luda,^{1,†} V. Kaushal,¹
J. Schulz,¹ D. von Lindenfels,¹ F. Schmidt-Kaler,¹ and U. G. Poschinger^{1,‡}

¹*Institut für Physik, Universität Mainz, Staudingerweg 7, 55128 Mainz, Germany*

We demonstrate a SWAP gate between laser-cooled ions in a segmented microtrap via fast physical swapping of the ion positions. This operation is used in conjunction with qubit initialization, manipulation and readout, and with other types of shuttling operations such as linear transport and crystal separation and merging. Combining these operations, we perform quantum process tomography of the SWAP gate, obtaining a mean process fidelity of 99.5(5)%. The swap operation is demonstrated with motional excitations below 0.05(1) quanta for all six collective modes of a two-ion crystal, for a process duration of 42 μ s. Extending these techniques to three ions, we reverse the order of a three-ion crystal and reconstruct the truth table for this operation, resulting in a mean process fidelity of 99.96(13)% in the logical basis.

PACS numbers: 37.10.Ty, 03.67.Lx, 42.50.Dv

I. INTRODUCTION

The last decade has seen substantial progress towards scalable quantum computing with trapped ions. Gate fidelities reach fault-tolerance thresholds [1], and first steps towards decoherence-free qubits were demonstrated [2]. Moreover, microfabricated ion traps continue to mature as an experimental low-noise environment [3, 4] hosting multi-qubit systems [5, 6]. In the seminal proposal [7] for such *quantum CCD chip*, scalability is reached through ion shuttling operations, where trapped-ion qubits are moved between different trap sites. Since the first demonstration of shuttling [8], the development of trap control hardware has progressed [9, 10]. This has led to demonstrations of fast ion shuttling at low motional excitation [11, 12].

It is an open question if a trapped-ion quantum computer should be based on large processing units hosting thousands of qubits [13, 14] or on a modular architecture of medium-sized nodes with photonic interconnectivity [15]. With current technology, the possibilities for high-fidelity control of ion strings consisting of more than a few ions are limited, such that ion shuttling is required in either case. For universal quantum computation, two-qubit gates need to be performed between arbitrary pairs of ions, such that reordering ion strings becomes necessary. Furthermore, if multiple ion species [16] are employed for sympathetic cooling [17] or ancilla-based syndrome readout via inter-species gates [18, 19], deterministic ion reconfiguration is ultimately required.

To that end, ion traps bearing junctions with T [20], X [21, 22] or Y [23] geometry have been developed and

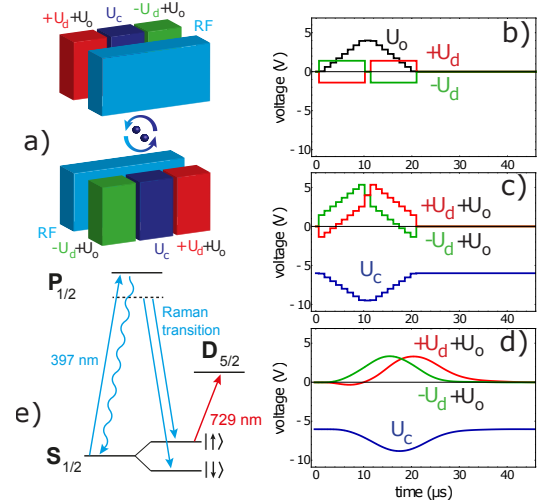


FIG. 1. Ion swapping in a segmented trap. **a)** shows the relevant trap electrodes, indicating how the trapping voltage U_c , diagonal voltage U_d and offset voltage U_o controlling the process are applied. Panels **b)** and **c)** show the voltage ramps in the form of discrete samples, as they are programmed to the arbitrary waveform generator. Here, **b)** shows U_d and U_o , while **c)** shows the actual electrode voltages. Panel **d)** shows the voltage ramps, measured after the low-pass filter, which leads to smoothing and delay of the ramps. **e)** shows the relevant part of the level scheme of $^{40}\text{Ca}^+$.

tested. Junctions increase the trap design complexity and allow only for sequential ion transport. Shuttling through junctions may yield large motional excitations, precluding the execution of two-qubit gates. In this work, we perform ion reordering via on-site swapping of ions through application of suitable electric potentials. The advantages of this operation are that it does not require sophisticated electrode structures, and that parallel multi-site swappings may be performed. In contrast to reordering via laser-driven SWAP gates, physical ion swapping does not require laser beams and can therefore be performed at any trap site. Furthermore, the physical SWAP operation does not affect the internal (qubit)

* Present address: LIAF - Laboratorio de Iones y Atomos Frios, Departamento de Fisica & Instituto de Fisica de Buenos Aires, 1428 Buenos Aires, Argentina

† Present address: DEILAP, CITEDEF & CONICET, J.B. de La Salle 4397, 1603 Villa Martelli, Buenos Aires, Argentina

‡ poschin@uni-mainz.de

states, such that virtually perfect operation fidelities are readily obtained. While it was shown [24] that segmented traps allow for ion swapping, we demonstrate this process on fast timescales, comparable to qubit operation times. Motional excitation is avoided, such that the ions stay within the Lamb-Dicke regime for all collective modes of vibration of a two-ion crystal. To highlight that this operation is deterministic and that it can be used in conjunction with other qubit operations, we integrate it within a sequence of shuttling, separation [12, 25, 26] and merging operations and qubit manipulations to realize quantum process tomography of the SWAP gate. By performing the swap operation on ground-state cooled ions and combining it with qubit manipulations, we demonstrate its potential use for scalable quantum logic.

II. EXPERIMENTAL SETUP

For our experiments, we trap $^{40}\text{Ca}^+$ ions in a segmented Paul trap similar to the design from [27]. Qubits are encoded in the Zeeman sublevels of the ground state $|\downarrow\rangle \equiv |S_{1/2}, m_J = -\frac{1}{2}\rangle$ and $|\uparrow\rangle \equiv |S_{1/2}, m_J = +\frac{1}{2}\rangle$. An external magnetic field lifts the degeneracy by $2\pi \times 10.4$ MHz. The ions are laser cooled on the $S_{1/2} \leftrightarrow P_{1/2}$ cycling transition near 397 nm. Qubit initialization with a fidelity $>99.8\%$ is achieved via optical pumping utilizing the narrow $S_{1/2} \leftrightarrow D_{5/2}$ quadrupole transition near 729 nm [28]. For qubit manipulation, we employ stimulated Raman transitions mediated by a co-propagating pair of laser beams near 397 nm, detuned by $2\pi \times 250$ GHz from the cycling transition. For sideband cooling and measurements of the motional state, we employ pairwise orthogonally propagating beams, where the difference wavevector is aligned parallel (orthogonal) to the trap axis, providing coupling to axial (radial) modes of oscillation. Qubit readout is accomplished by spin-selective electron shelving to the metastable $D_{5/2}$ state, followed by detection of state-dependent fluorescence with a photomultiplier tube [28]. All lasers are directed at the laser interaction zone (LIZ), see Fig. 3. As the beams driving the single-qubit operations are co-propagating, and the laser near 729 nm for electron shelving is directed perpendicularly to the trap axis, both operations are insensitive to axial ion motion. Control of the ion motion is achieved by individual supply of the trap electrodes by a fast multichannel arbitrary waveform generator [11, 25] at update rates of up to 2.5 MSamples/s, where each signal line has a second-order low-pass filter with a cutoff frequency of $2\pi \times 50$ kHz.

III. FAST SWAP OPERATION

The on-site swapping process of a two-ion crystal is depicted in Fig. 1. We start with the crystal axially confined by applying a voltage U_c to the trapping electrodes (blue segments in Fig. 1). Control over the ion

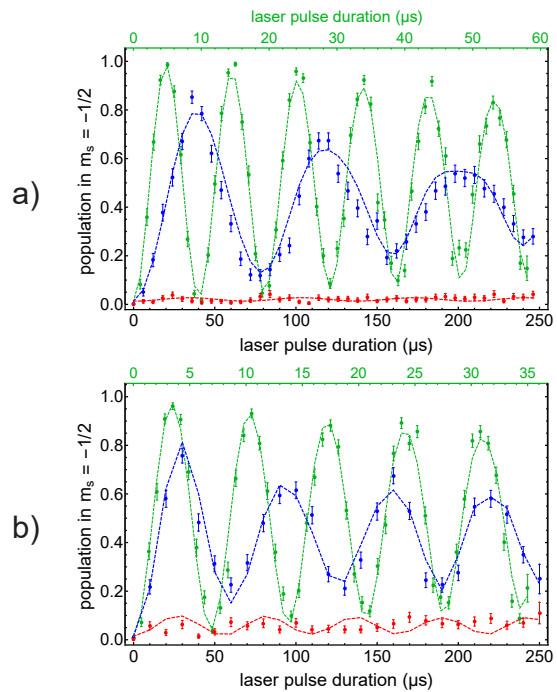


FIG. 2. Rabi oscillation data probed after swapping for verification of low excitation: **a)** shows data for the axial stretch mode, while **b)** shows data for the lower-frequency radial rocking mode. In both panels, the blue (red) points correspond to the blue (red) motional sideband, while the green points correspond to the carrier transition. The dashed lines are fits using a model assuming oscillatory excitation. All curves indicate the probability for having at least one of the ions' state flipped to $|\downarrow\rangle$. Note that the time axis for the carrier data is scaled differently (upper axis ticks). Each data point corresponds to 200 state interrogations.

crystal rotation is achieved via a diagonal, symmetry-breaking dc quadrupole potential, generated by ramping up a voltage $+(-)U_d$ to the electrodes neighboring the trap site, shown in green (red) in Fig. 1. The polarity on the electrode pair left of the trapping site is inverted as compared to the electrode pair to the right. With the diagonal potential applied, the trapping voltage U_c is decreased, and a positive offset voltage U_o is ramped up at all neighboring segments. The corresponding increase of the axial confinement drives the ion crystal through a structural transition from horizontal to vertical alignment. Simultaneously, the diagonal potential generated by U_d is ramped down to 0 V. With the ions vertically aligned, the process is conducted in reverse order, with inverted polarity of the diagonal voltage U_d .

We optimize the voltage ramps by probing the final motional excitation on the vibrational modes which are most affected, i.e. the axial *stretch* and the lower frequency radial *rocking* mode. The motional excitation is measured by driving Rabi oscillations on the red and blue motional sidebands pertaining to the respective modes of vibration. Each mode is cooled close to the ground state via sideband cooling before the swapping operation, reaching mean phonon numbers between 0.016(4) (axial

stretch mode) and 0.37(1) (lower frequency radial COM mode). Rabi oscillations are recorded over pulse areas of up to 8π pertaining to the blue sideband ground-state Rabi frequency. Fits assuming oscillatory excitation, i.e. a coherent state of the corresponding mode, reveal the mean phonon number [11, 25, 29].

Initially, a trapping voltage $U_c = -6$ V yields horizontal crystal alignment at an axial center-of-mass (COM) vibrational frequency of $2\pi \times 1.488$ MHz. The radial COM frequencies are $2\pi \times 1.927$ MHz and $2\pi \times 3.248$ MHz. We define the dimensionless time $\tau = t/T$ for the total swapping time T . The least motional excitation is found for the following ramp parameters: The diagonal voltage U_d is ramped up rapidly within $\tau = 0.05$, to an optimum value of 1.4 V. For driving the ion crystal into vertical alignment, the axial COM frequency has to exceed the lower radial COM frequency. To that end, U_c is ramped down to -9.5 V, while at the same time an additional offset voltage $U_o = +4$ V is ramped up at all neighboring electrodes. Both U_c and U_o are ramped within $\tau = 0.05$ to $\tau = 0.45$. The polarity change of the diagonal voltage U_d happens during $\tau = 0.45$ to $\tau = 0.55$. The resulting voltage ramps are depicted in Fig. 1.

The swapping operation was tested for increasing times T , until we found the shortest time with negligible motional excitation of $T = 22 \mu\text{s}$, which -including the filters- corresponds to an actual duration of $42 \mu\text{s}$. We measure the mean phonon number increase for all modes, and compare to reference measurements directly after sideband cooling, see table I. For the axial modes, we find mean phonon number increases of 0.05(1) on the COM mode and 0.013(6) on the stretch mode. For the lower-frequency radial modes, corresponding to the plane in which the crystal rotates, we obtain 0.03(2) on the COM mode and 0.04(2) on the rocking mode. The higher-frequency radial mode, which is least affected from the swapping, features 0.02(1) on the COM and 0.01(1) on the rocking mode. Rabi oscillation data probed after swapping is shown in Fig. 2.

Linear transport of ions along the trap axis is performed by gradually reducing the negative dc trapping voltage of $U_c = -6$ V at the initial segment to 0 V, while applying a trapping voltage at the neighboring destination segment. We perform adiabatic transport at a duration of $28 \mu\text{s}$ per trap segment pair, spaced by $200 \mu\text{m}$. Transport over more than one segment pair is performed by concatenation of these operations. Separation/merging operations require switching between single- and double-well potentials, where the transient low axial confinement causes excitation [26]. We employ tailored voltage waveforms and accurate cancellation of residual forces along the trap axis, enabling separation/merging of two-ion crystals within $100 \mu\text{s}$ at excitations of 5(2) phonons per ion [25].

motional mode	$\omega/2\pi$ (MHz)	η	\bar{n}	\bar{n} increase
axial c.o.m.	1.488	0.127	0.082(6)	-
axial c.o.m. with SWAP		0.129	0.131(7)	0.049(9)
axial stretch	2.578	0.100	0.016(4)	-
axial stretch with SWAP		0.099	0.029(5)	0.013(6)
radial 1 c.o.m.	1.927	0.069	0.365(13)	-
radial 1 c.o.m. with SWAP		0.070	0.394(13)	0.029(18)
radial 1 rocking	1.195	0.090	0.14(10)	-
radial 1 rocking with SWAP		0.090	0.18(11)	0.041(15)
radial 2 c.o.m.	3.248	0.066	0.099(9)	-
radial 2 c.o.m. with SWAP		0.066	0.115(10)	0.015(14)
radial 2 rocking	2.875	0.072	0.069(8)	-
radial 2 rocking with SWAP		0.072	0.081(7)	0.012(10)

TABLE I. Measured phonon numbers on the six collective motional modes of a two ion crystal with and without the swapping operation. The column \bar{n} increase is the difference between a measurement with and without swapping and corresponds to the motional excitation from the swapping.

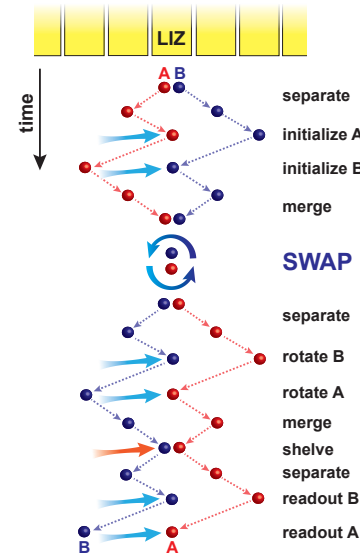


FIG. 3. Experimental quantum process tomography sequence for characterizing the SWAP operation. Each of the qubits A and B is shuttled to the laser interaction zone for initialization laser pulses, followed by a fast SWAP operation and subsequent individual qubit rotations. The SWAP operation is realized in $42 \mu\text{s}$. Finally, the state is read out via electron shelving and fluorescence detection.

IV. PROCESS TOMOGRAPHY OF TWO-ION SWAP

The sequence for process tomography is depicted in Fig. 3. First, the two-ion crystal is prepared by Doppler cooling and pumping in the LIZ. After separation, each

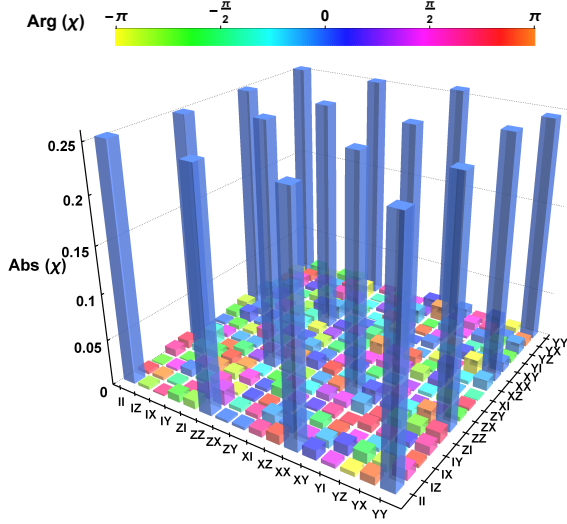


FIG. 4. Reconstructed process χ -matrix for the SWAP operation. The absolute value of each matrix element is represented by the bar height, the phase is indicated by the color. The 16 elements which match the ideal absolute value of 0.25 have a controlled phase of $\arg(\chi_{ij}) \approx 0$. All other elements are close to the ideal value of zero and have random phases. Each of the 144 preparation/measurement settings is probed on average 1260 times.

qubit is individually shuttled into the LIZ, where one of the operations $\{1, R_X(\pi/2), R_Y(\pi/2), R_X(\pi)\}$ is applied to bring the respective qubit to the state $\{|\uparrow\rangle, |\uparrow\rangle - i|\downarrow\rangle, |\uparrow\rangle - |\downarrow\rangle, |\downarrow\rangle\}$. The ions are merged in the LIZ, where the swapping takes place. The crystal is again separated, and the ions are individually exposed to the analysis pulses $\{1, R_X(\pi/2), R_Y(\pi/2)\}$ for measuring the operators $\{\sigma_z, \sigma_y, \sigma_x\}$. After another merging operation in the LIZ, the population transfer $|\uparrow\rangle \leftrightarrow |D_{5/2}\rangle$ takes place. The ions are again separated and individually shuttled to the LIZ, where state-dependent fluorescence is observed. Both qubits are shelved *before* fluorescence detection, to avoid depolarization of a remotely stored qubit from scattered light near 397 nm during the readout of the other qubit. The analysis laser pulses have to be corrected for phases arising from axial ion movement in the inhomogeneous magnetic field. Qubit i located at axial position $x_i(t)$ at time t accumulates a phase which is determined by the deviation of the magnetic field from its value at the LIZ, $\Delta B(x)$:

$$\phi_i = \frac{\mu_B g J}{\hbar} \int_{t_i^{(i)}}^{t_i^{(a)}} \Delta B(x_i(t)) dt. \quad (1)$$

Here, $t_i^{(i)}$ denotes the instant of the state preparation for qubit i and $t_i^{(a)}$ denotes the instant of its analysis pulse. The magnetic field inhomogeneity along the trap axis is mapped out by using a single ion as a probe: Initialized in a superposition state, it is shuttled to the destination site x and kept on hold for variable time t . After shuttling back to the LIZ, a refocusing π -pulse is applied, followed by another wait time of duration t with the ion placed

at the LIZ. Finally, state tomography reveals the accumulated phase $\phi(x, t) = \frac{\mu_B g J}{\hbar} \Delta B(x) \cdot t + \phi_0$, where ϕ_0 is a constant phase accumulated during the shuttling. By performing such measurements for different phase accumulation times t at different locations x , we map out the qubit frequency shift across segments 18-22 with a mean accuracy of about $2\pi \times 1$ Hz. With the positions $x_i(t)$ computed from the sequence data and simulated electrostatic trap potentials [31], the phases ϕ_i can be also computed and used for correcting the phases of the analysis pulses. For each of the 16 prepared states, 9 measurements are performed, each independently repeated 1000 times. A density matrix is obtained via linear inversion for each input state. From these density matrices, the process χ -matrix is reconstructed via a second linear inversion. Computing the trace norm $\text{Tr}(\chi_{meas}^\dagger \chi_{ideal})$, we find a mean process fidelity of 98.1(5)%. Performing process tomography without SWAP operation, we obtain a mean process fidelity of 98.7(4)%. Thus, on the given level of accuracy, we conclude that the SWAP operation does not significantly affect the measured process fidelity, which is limited mainly by readout errors and systematic errors of the correction phases. Readout errors have been independently measured using a sequence without the SWAP operation, for details see the supplemental material [30]. The errors are dominated by the limited lifetime of the metastable $D_{5/2}$ state, imperfect electron shelving and state initialization. Applying correction for readout errors to the SWAP data, we obtain a mean process fidelity of 99.5(5)%. The resulting χ -matrix is displayed in Fig. 4.

V. REORDERING OF A THREE-ION CRYSTAL

The techniques described above are extended to three qubits, where we demonstrate reordering from configuration ABC to configuration CBA . The experimental sequence is sketched in Fig. 5, the full detailed sequence can be found in the supplemental material [30].

Rather than performing quantum process tomography, we restrict the measurements to the logical (Z) basis, thus we reconstruct the truth table of the reordering operation. Starting from a three-ion crystal ABC in the LIZ, we separate into AB and C by performing the separation with a properly adjusted axial bias field [12]. Ion C is moved to segment 26, then ions AB are moved back into the LIZ, where separation into A and B takes place. Then, A , B and C are subsequently moved into the LIZ and initialized to either $|\uparrow\rangle$ or $|\downarrow\rangle$. Now, the ions are merged pairwise at the LIZ, where swapping and subsequent separation take place. The respective third ion is stored six segments away to the left or right, such that its trapping potential does not affect the separation/merging and swapping operations. The three subsequent swaps $AB \rightarrow BA$, $AC \rightarrow CA$ and $BC \rightarrow CB$ establish the desired order CBA . Then, the ions are individually moved to the LIZ for shelving, and then indi-

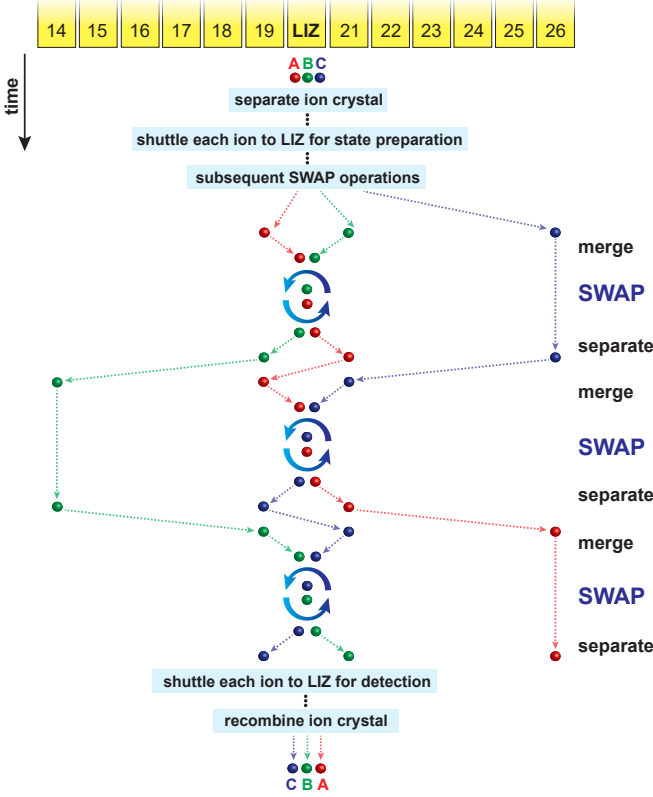


FIG. 5. Experimental sequence for the reordering of a three-ion crystal from configuration ABC to configuration CBA by employing three consecutive SWAP operations. The separation, merging, state preparation and state detection operations at the beginning and the end of the sequence are omitted in this sketch, see full text for details.

vidually moved to the LIZ for fluorescence readout. We measure the final spin configuration for 8 different input states. The resulting truth table is shown in Fig. 6. We obtain a mean fidelity of 98.47(9)% in the logical basis. The mean fidelity with readout error correction is 99.96(13)%. The sequence consists of three separation, three merging, three swapping and 30 linear transport operations. The execution time of this process is 5.7 ms, where 93% of which is devoted to shuttling operations.

VI. OUTLOOK

In conclusion, we have demonstrated basic functionality of a quantum processing unit based on different shuttling operations, including qubit register reconfiguration. It was shown that operations such as coherent manipulation and readout are not affected by swapping and other shuttling operations. In future experiments, the time required for such shuttling operations will be substantially reduced by several measures: Compensation of filter-induced waveform distortions and a novel waveform generator with a voltage range of ± 40 V will enable faster shuttling and swapping at larger radial trap frequencies.

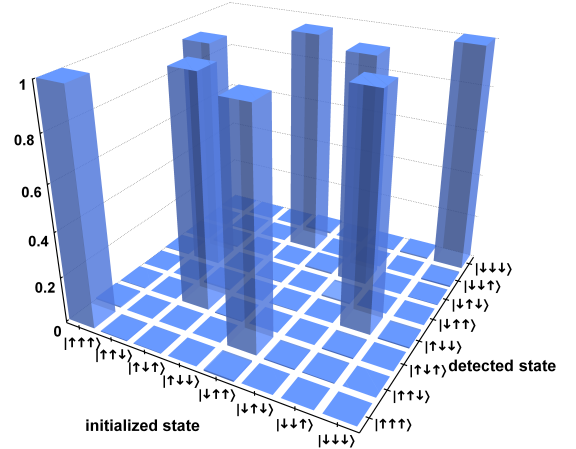


FIG. 6. Measured truth table for three-ion reconfiguration from ABC to CBA , using three consecutive two-ion SWAP operations. Each ion was prepared in either $|\uparrow\rangle$ or $|\downarrow\rangle$. Each input state is probed on average 2500 times. The measured probability to detect a particular state is represented by the height of the bars.

Furthermore, control techniques [32, 33] may be applied to enable faster shuttling.

VII. ACKNOWLEDGEMENTS

ACKNOWLEDGMENTS

The research is based upon work supported by the Office of the Director of National Intelligence (ODNI), Intelligence Advanced Research Projects Activity (IARPA), via the U.S. Army Research Office grants W911NF-10-1-0284 and W911NF-16-1-0070. We acknowledge financial support by the Bundesministerium für Bildung und Forschung via IKT 2020 (Q.com). The views and conclusions contained herein are those of the authors and should not be interpreted as necessarily representing the official policies or endorsements, either expressed or implied, of the ODNI, IARPA, or the U.S. Government. The U.S. Government is authorized to reproduce and distribute reprints for Governmental purposes notwithstanding any copyright annotation thereon. Any opinions, findings, and conclusions or recommendations expressed in this material are those of the author(s) and do not necessarily reflect the view of the U.S. Army Research Office.

VIII. APPENDIX A: READOUT ERROR CORRECTION FOR THE PROCESS TOMOGRAPHY

For the measurements on full process tomography for two ions, 16 different settings for preparation $s = \{s_1, s_2\}$ with $s_i \in \{|\uparrow\rangle, |\uparrow\rangle - i|\downarrow\rangle, |\uparrow\rangle - |\downarrow\rangle, |\downarrow\rangle\}$ and 9 different setting for detection $d = \{d_1, d_2\}$ with $d_i \in \{Z, Y, X\}$ are probed. Each setting (s, d) is probed on average

N times. Small fluctuations of the measurement numbers between different settings arise from postselection removal of events where ions are lost or crystal melting occurs, these fluctuations are ignored in the following. For each setting, $N_f^{(s,d)}$ events out of N detections yield the fluorescence result $f = \{f_1, f_2\}$, where $f_i = \{\text{dark}, \text{bright}\}$. From this data, event frequencies $P_f^{(s,d)} = N_f^{(s,d)}/N$ are calculated. For a given preparation setting s , these frequencies are used for linear inversion to obtain the resulting density matrix $\rho^{(s)}$. The set of 16 resulting density matrices is used for a second linear inversion to obtain the resulting process matrix χ_{meas} . The process fidelity F with respect to the ideal process χ_{ideal} is then given by the trace norm $F = \text{Tr}(\chi_{\text{ideal}}^\dagger \chi_{\text{meas}})$.

We estimate confidence intervals for the mean process fidelity via parametric bootstrapping. For this, we generate 500 instances of random measurement data. For each instance, we use the event frequencies $P_f^{(s,d)}$ to generate multivariate random integers $\tilde{N}_f^{(s,d)}$, drawn from a multinomial distribution $f(\{\tilde{N}_f^{(s,d)}\}, \{P_f^{(s,d)}\})$, where $\sum_f \tilde{N}_f^{(s,d)} = N$ and $\sum_f P_f^{(s,d)} = 1$. These random event numbers serve to calculate random event frequencies $\tilde{P}_f^{(s,d)}$, which are used in turn to generate random process matrices $\tilde{\chi}_{\text{meas}}$. Averaging over the 500 instances, we obtain the mean process fidelity along with a confidence interval.

In order to correct for readout errors, we perform the same procedure *without* SWAP operation, obtaining the event frequencies $\tilde{P}_f^{(s,d)}$, the density matrices $\tilde{\rho}^{(s)}$ and the process matrix $\tilde{\chi}_{\text{meas}}$. We restrict ourselves to the prepared spin configurations which are eigenstates of the Z_i operators, $s' \in \{|\uparrow\uparrow\rangle, |\uparrow\downarrow\rangle, |\downarrow\uparrow\rangle, |\downarrow\downarrow\rangle\}$. The diagonal elements of the reconstructed density matrices $\tilde{\rho}_{kk}^{(s')}$ indicate the conditional probabilities to detect fluorescence result f_k for preparation setting s' and detection setting $d = Z_1 Z_2$. Under the assumption of uncorrelated readout errors, these probabilities $\tilde{\rho}_{kk}^{(s')}$ are products of the probabilities to detect dark/bright events for the ion in $|\uparrow\rangle/|\downarrow\rangle$ for each ion i :

$$\begin{aligned} \tilde{\rho}_{kk}^{(s')} &= P_{f_k}^{(s', Z_1 Z_2)} \\ &= p_1(f_{k,1}|s'_1) \cdot p_2(f_{k,2}|s'_2), \end{aligned} \quad (2)$$

This holds under the assumption of perfect state preparation. It further holds that

$$\begin{aligned} p_i(\text{dark}_i|\uparrow_i) &\lesssim 1 \\ p_i(\text{bright}_i|\uparrow_i) &\gtrsim 0 \\ p_i(\text{dark}_i|\downarrow_i) &\gtrsim 0 \\ p_i(\text{bright}_i|\downarrow_i) &\lesssim 1 \\ p_i(\text{dark}_i|\uparrow_i) + p_i(\text{bright}_i|\uparrow_i) &= 1 \\ p_i(\text{dark}_i|\downarrow_i) + p_i(\text{bright}_i|\downarrow_i) &= 1 \end{aligned} \quad (3)$$

We calculate the readout probabilities $p_i(f_{k,i}|s_i)$ by using the former normalization, e.g.

$$\begin{aligned} p_1(\text{dark}_1|\uparrow_1) &= \frac{1}{2} P_{\text{dark}_1 \text{dark}_2}^{(\uparrow_1 \uparrow_2, Z_1 Z_2)} \\ &+ \frac{1}{2} P_{\text{dark}_1 \text{bright}_2}^{(\uparrow_1 \uparrow_2, Z_1 Z_2)} \\ &+ \frac{1}{2} P_{\text{dark}_1 \text{dark}_2}^{(\uparrow_1 \downarrow_2, Z_1 Z_2)} \\ &+ \frac{1}{2} P_{\text{dark}_1 \text{bright}_2}^{(\uparrow_1 \downarrow_2, Z_1 Z_2)} \end{aligned} \quad (4)$$

These readout probabilities are used to form the readout probability matrix M ,

$$M_{jk} = p_1(f_{j,1}|s'_{k,1}) \cdot p_2(f_{j,2}|s'_{k,2}). \quad (5)$$

This matrix determines the observed event frequencies *including* readout errors $\tilde{P}_f^{(s,d)}$ from the event frequencies $\hat{P}_f^{(s,d)}$ determined by the density matrix describing the state *before* readout:

$$\tilde{P}_f^{(s,d)} = M \cdot \hat{P}_f^{(s,d)}, \quad (6)$$

where the index f is running over the different observable fluorescence results. Thus, we can obtain the corrected event frequencies from

$$\hat{P}_f^{(s,d)} = M^{-1} \cdot \tilde{P}_f^{(s,d)}. \quad (7)$$

The corrected event frequencies can then be used for obtaining the process matrix as above, and parametric bootstrapping can be applied. From the fidelities obtained from parametric bootstrapping with the identity operation, we indeed obtain unit fidelity within the statistical error. This confirms the validity of the assumptions that the errors of preparation and single qubit rotations are insignificant as compared to readout errors, and that the readout errors are uncorrelated.

We can thus apply the readout error correction to the tomography data for the SWAP gate:

$$\hat{P}_f^{(s,d)} = M^{-1} \cdot \tilde{P}_f^{(s,d)}. \quad (8)$$

Performing parametric bootstrapping for this case, we also generate a random instance of the identity data along with the random instance of the SWAP data, such that both M^{-1} and $\tilde{P}_f^{(s,d)}$ are random quantities. This way, we take the statistical errors of the readout correction into account.

From the identity measurement, we infer the following readout probabilities:

$$\begin{aligned} p_1(\text{dark}_1|\uparrow_1) &= 0.9941(7) \\ p_2(\text{dark}_2|\uparrow_2) &= 0.9924(9) \\ p_1(\text{bright}_1|\downarrow_1) &= 0.9888(10) \\ p_2(\text{bright}_2|\downarrow_2) &= 0.9945(7) \end{aligned} \quad (9)$$

The resulting corrected process χ -matrix is visualized in Fig. 4 of the main manuscript. Here, we additionally present the numerical data in Fig. 7:

For the three-ion measurements, we proceed in a similar way. There are however only 8 preparation settings, only one detection setting (Z) and 8 fluorescence combinations. The observed event frequencies can be directly

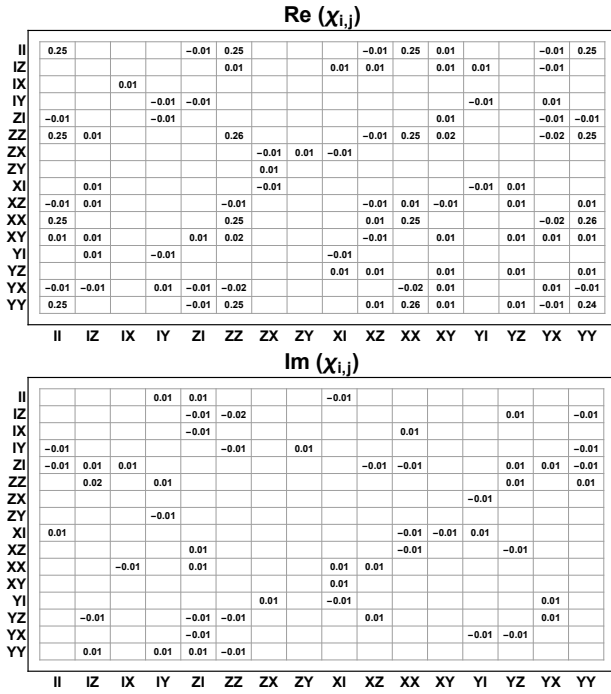


FIG. 7. Real and imaginary part of the χ -matrix which was obtained in the quantum process tomography shown in Fig. 5 of the main manuscript. The absolute value of empty fields is smaller than 0.01.

interpreted as elements of the process matrix in the truncated basis, such that no linear inversions are carried out and the readout correction can be directly applied. For the process fidelity in the truncated basis, we report the fidelities with significantly reduced statistical error, despite the fact that roughly the same number of measurements are used for each preparation setting. The reason for this is that we prepare *and* detect only in the logical basis in this case, which leads to detection event probabilities always close to either 0 or 1. This leads to reduced shot noise.

IX. APPENDIX B: THREE-ION CRYSTAL RECONFIGURATION

Here, we describe in detail how the reordering of the three-ion crystal ABC to CBA is accomplished. The experimental sequence is sketched in Fig. 8. The sequence starts with a three-ion crystal, trapped in a harmonic potential at electrode 20 which is called laser interaction zone (LIZ) since all lasers are targeted at this electrode. The sequence is partitioned in three sequences: *pre-sequence*, *main-sequence* and *post-sequence*. First, the pre-sequence is executed. Then, the main-sequence is executed and repeated 90 times. After the final repetition of the main sequence, the post-sequence is executed.

Pre-sequence: At the beginning of the pre-sequence,

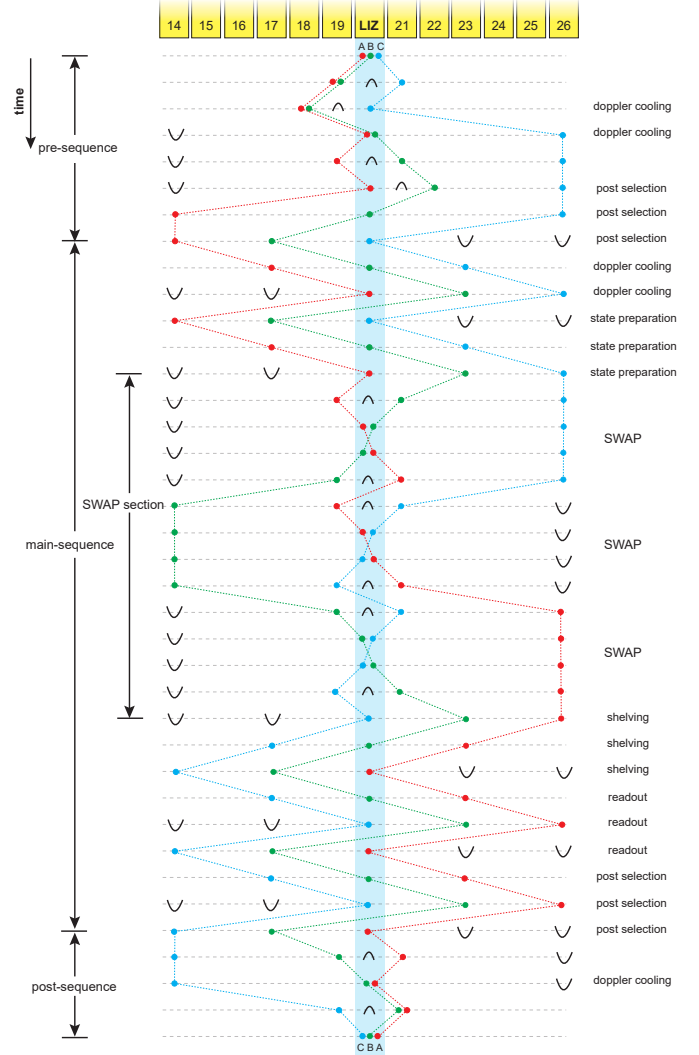


FIG. 8. Experimental sequence for the reconfiguration of a three ion crystal from ABC to CBA by using three consecutive two-ion SWAP operations. Black potential wells or barriers are applied to achieve a symmetric potential along the trap axis, thus placing the ions in the center of the laser beams.

the three-ion crystal is Doppler cooled with a 397 nm laser. The crystal is then split by applying the separation voltage ramps with an additional calibrated axial bias field, such that the two ions A and B deterministically move to the left and ion C moves to the far right. The two-ion crystal AB is then shuttled to the LIZ, where Doppler cooling is applied. A potential well at electrode 14 is generated, which is of the same depth as on electrode 26, such that the potential well at the LIZ is properly centered and symmetric. The two-ion crystal AB is then separated, and each of the three ions A , B and C is shuttled individually to the LIZ for Doppler cooling and detection of ion loss events. In this part of the sequence, only **sequential transports** are used, where one transport corresponds to the movement of one ion from one electrode to a neighboring electrode, while the other ions remain at their position.

shuttling operation	duration (μ s)	quantity
separation	260	2
sequential transport	120	31
total shuttling operation time	4.2 ms	
total sequence duration	39.7 ms	
percentage of shuttling operations	10.6 %	

TABLE II. Operations used in the **pre-sequence**.

operation	duration (μ s)	quantity
separation	260	3
merging	260	3
sequential transport	120	30
parallel transport (3 ions)	100	48
SWAP	42	3
doppler cooling	2500	17
fluorescence detection	1200	6
shelving	600	3
other operations (spin init., dwell times, compensation pot. ramps)	1700	-
total shuttling operation time	10.1 ms	
total sequence duration	63.5 ms	
percentage of shuttling operations	15.9 %	

TABLE III. Shuttling operations used in the **main-sequence**.

Main sequence: In the main sequence, each ion is shuttled individually to the LIZ for Doppler cooling. Afterwards, each ion is optically pumped at the LIZ for state initialization to either $|\uparrow\rangle$ or $|\downarrow\rangle$. The total state of the three ions is then initialized to one of eight possible configurations. Thus, the entire sequence is performed for each of the eight possible input states.

Subsequently, the reordering of the three ions via two-ion swap operations is carried out. At first, the ions A and B are merged in the LIZ and the crystal swapping operation is executed. Thus, the order of the ions along the trap axis is changed to BAC . The two-ion crystal is then separated and the ions A and C are shuttled to the LIZ and merged together. Another swap operation is conducted, such that the order of the ions is changed to BCA . After that, the ions B and C are merged at the LIZ for a final swap operation to yield the desired order of CBA .

Afterwards, each ion is shuttled to the LIZ for electron shelving and subsequent detection of the spin state. It is important to perform the shelving operation on the ions *before* the detection operation takes place. The latter is done by illumination with 397 nm laser light, as residual stray light on an un-shelved ion can depolarize the internal state, even if the ion is located several electrodes away.

In the main sequence, **parallel transports** are used, where all three separately trapped ions move simultaneously from one site to another. One parallel transport operation corresponds to the simultaneous movement of each of the ions from their initial electrode to one neighboring electrode.

Post-sequence: In the post-sequence, the individually trapped ions C , B and A are shuttled to the LIZ for post-selection of ion loss events. Afterwards, the ions A and B are merged, followed by a merging of the ion C to the two-ion crystal BA , thus yielding the three-ion crystal CBA .

shuttling operation	duration (μ s)	quantity
merging	260	2
sequential transport	120	9
total shuttling operation time	1.6 ms	
total sequence duration	6.6 ms	
percentage of shuttling operations	24.3 %	

TABLE IV. Shuttling operations used in the **post-sequence**.

The duration of the entire sequence amounts to 109.8 ms, while the most relevant part - the main sequence - takes 38.6 ms. The tables II - V show more details on the shuttling operations which were employed. The shuttling operations require 23 % of the total duration of the main-sequence. In the following we explain the reason for this overhead and how to reduce it.

The swap operations require trap operation at a rather low RF level to make the swapping operation feasible, as the DC supply is limited to ± 10 V, and the axial confinement has to exceed the radial confinement in one direction during the swap operation. The low-frequency radial mode is only at $\omega/2\pi = 1.93$ MHz. While we have verified that the excitation from the swapping operation is negligible, the linear transport operations add a slight amount of excitation if executed at low RF trap-drive amplitude. In the two-ion process tomography, this effect is negligible since only a few shuttling operations are used. By contrast, for the three-ion crystal reconfiguration, the amount of transport operations is much larger, such that we need to execute some of the shuttling operations more slowly for optimum readout fidelity. In contrast to the two-ion measurements, the separation and merging operations are executed slower: 260μ s as compared to 100μ s. Also, the sequential transports are slower: 120μ s as compared to 28μ s. This will be improved in future experiments, such that swapping can be executed at higher RF levels.

In Fig. 9, we show the data obtained for the three-ion measurements, which is also displayed as a bar chart in

shuttling operation	duration (μ s)	quantity
separation	260	5
merging	260	5
sequential transport	120	70
parallel transport (3 ions)	100	48
SWAP	42	3
total shuttling operation time	15.9 ms	
total sequence duration	109.8 ms	
percentage of shuttling operations	14.5 %	

TABLE V. Shuttling operations and timings used in the **entire sequence**.

operation	duration (μ s)	quantity
separation	260	3
merging	260	3
sequential transport	120	30
SWAP	42	3
other operations (dwell times, compensation pot. ramps)	400	-
total shuttling operation time	5.3 ms	
total section duration	5.7 ms	

TABLE VI. Shuttling operations used in the **SWAP**-section.

the main manuscript.

$ \uparrow\uparrow\uparrow\rangle$	1.001	0.007	0.003	0	0.002	0	0	0
$ \uparrow\uparrow\downarrow\rangle$	-0.004	0	0	0	0.998	0.006	0.003	0
$ \uparrow\downarrow\uparrow\rangle$	-0.002	0	1.002	0.007	0	0	0	0.001
$ \uparrow\downarrow\downarrow\rangle$	0	0	-0.004	0	-0.002	0	0.998	0.009
$ \downarrow\uparrow\uparrow\rangle$	-0.007	0.995	0	0.003	0	0.007	0	0
$ \downarrow\uparrow\downarrow\rangle$	0	-0.005	0	0	-0.007	1.001	0	0.003
$ \downarrow\downarrow\uparrow\rangle$	0	-0.004	-0.006	0.999	0	0	0	0.006
$ \downarrow\downarrow\downarrow\rangle$	0	0	0	-0.006	0	-0.002	-0.007	1.002
	$ \uparrow\uparrow\uparrow\rangle$	$ \uparrow\uparrow\downarrow\rangle$	$ \uparrow\downarrow\uparrow\rangle$	$ \uparrow\downarrow\downarrow\rangle$	$ \downarrow\uparrow\uparrow\rangle$	$ \downarrow\uparrow\downarrow\rangle$	$ \downarrow\downarrow\uparrow\rangle$	$ \downarrow\downarrow\downarrow\rangle$

FIG. 9. Measured three ion truth table. Small negative values arise due to the readout error correction.

-
- [1] C. J. Ballance, T. P. Harty, N. M. Linke, M. A. Sepiol, and D. M. Lucas, (2015), arXiv:1512.04600 [quant-ph].
- [2] D. Nigg, M. Müller, E. A. Martinez, P. Schindler, M. Hennrich, T. Monz, M. A. Martin-Delgado, and R. Blatt, *Science* **345**, 302 (2014).
- [3] D. A. Hite, Y. Colombe, A. C. Wilson, K. R. Brown, U. Warring, R. Jördens, J. D. Jost, K. S. McKay, D. P. Pappas, D. Leibfried, and D. J. Wineland, *Phys. Rev. Lett.* **109**, 103001 (2012).
- [4] N. Daniilidis, S. Gerber, G. Bolloten, M. Ramm, A. Ransford, E. Ulin-Avila, I. Talukdar, and H. Häffner, *Phys. Rev. B* **89**, 245435 (2014).
- [5] J. P. Home, D. Hanneke, J. D. Jost, J. M. Amini, D. Leibfried, and D. J. Wineland, *Science* **325**, 1227 (2009).
- [6] C. D. Herold, S. D. Fallek, J. T. Merrill, A. M. Meier, K. R. Brown, C. Volin, and J. M. Amini, (2015), arXiv:1509.05378 [quant-ph].
- [7] D. Kielpinski, C. Monroe, and D. J. Wineland, *Nature* **417**, 709 (2002).
- [8] M. A. Rowe, A. Ben-Kish, B. DeMarco, D. Leibfried, V. Meyer, J. Beall, J. Britton, J. Hughes, W. M. Itano, B. Jelenkovic, C. Langer, T. Rosenband, and D. J. Wineland, *Quantum Inf. and Comput.* **2**, 257 (2002).
- [9] R. Bowler, U. Warring, J. W. Britton, B. C. Sawyer, and J. Amini, *Rev. Sci. Instrum.* **84**, 033108 (2013).
- [10] M. T. Baig, M. Johanning, A. Wiese, S. Heidbrink, M. Ziolkowski, and C. Wunderlich, *Rev. Sci. Instrum.* **84**, 124701 (2013).
- [11] A. Walther, F. Ziesel, T. Ruster, S. T. Dawkins, K. Ott, M. Hettrich, K. Singer, F. Schmidt-Kaler, and U. G. Poschinger, *Phys. Rev. Lett.* **109**, 080501 (2012).
- [12] R. Bowler, J. Gaebler, Y. Lin, T. R. Tan, D. Hanneke, J. D. Jost, J. P. Home, D. Leibfried, and D. J. Wineland, *Phys. Rev. Lett.* **109**, 080502 (2012).
- [13] A. M. Steane, *Quant. Inf. Comp.* **7**, 171 (2007).
- [14] B. Lekitsch, S. Weidt, A. G. Fowler, K. Mølmer, S. J. Devitt, C. Wunderlich, and W. K. Hensinger, (2015), arXiv:1508.00420 [quant-ph].
- [15] C. Monroe, R. Raussendorf, A. Ruthven, K. R. Brown, P. Maunz, L.-M. Duan, and J. Kim, *Phys. Rev. A* **89**, 022317 (2014).
- [16] J. P. Home, in *Advances in Atomic, Molecular, and Optical Physics*, Advances In Atomic, Molecular, and Optical Physics, Vol. 62, edited by P. R. B. Ennio Arimondo and C. C. Lin (Academic Press, 2013) pp. 231 – 277.
- [17] D. Kielpinski, B. E. King, C. J. Myatt, C. A. Sackett, Q. A. Turchette, W. M. Itano, C. Monroe, D. J. Wineland, and W. H. Zurek, *Phys. Rev. A* **61**, 032310 (2000).
- [18] C. J. Ballance, V. M. Schäfer, J. P. Home, D. J. Szwer, S. C. Webster, D. T. C. Allcock, N. M. Linke, T. P. Harty, D. P. L. A. Craik, D. N. Stacey, A. M. Steane, and D. M. Lucas, *Nature* **528**, 384 (2015).
- [19] T. R. Tan, J. P. Gaebler, Y. Lin, Y. Wan, R. Bowler, D. Leibfried, and D. J. Wineland, *Nature* **528**, 380 (2015).
- [20] W. K. Hensinger, S. Olmschenk, D. Stick, D. Hucul, M. Yeo, M. Acton, L. Deslauriers, C. Monroe, and J. Rabchuk, *Applied Physics Letters* **88**, 034101 (2006).
- [21] R. B. Blakestad, C. Ospelkaus, A. P. VanDevender, J. M. Amini, J. Britton, D. Leibfried, and D. J. Wineland, *Phys. Rev. Lett.* **102**, 153002 (2009).
- [22] K. Wright, J. M. Amini, D. L. Faircloth, C. Volin, S. C. Doret, H. Hayden, C.-S. Pai, D. W. Landgren, D. Denison, T. Killian, R. E. Shusher, and A. W. Harter, *New*

- Journal of Physics **15**, 033004 (2013).
- [23] G. Shu, G. Vittorini, A. Buikema, C. S. Nichols, C. Volin, D. Stick, and K. R. Brown, Phys. Rev. A **89**, 062308 (2014).
 - [24] F. Splatt, M. Harlander, M. Brownnutt, F. Zähringer, R. Blatt, and W. Hänsel, New Journal of Physics **11**, 103008 (2009).
 - [25] T. Ruster, C. Warschburger, H. Kaufmann, C. T. Schmiegelow, A. Walther, M. Hettrich, A. Pfister, V. Kaushal, F. Schmidt-Kaler, and U. G. Poschinger, Phys. Rev. A **90**, 033410 (2014).
 - [26] H. Kaufmann, T. Ruster, C. T. Schmiegelow, F. Schmidt-Kaler, and U. G. Poschinger, New Journal of Physics **16**, 073012 (2014).
 - [27] S. Schulz, U. Poschinger, F. Ziesel, and F. Schmidt-Kaler, New J. Phys. **10**, 045007 (2008).
 - [28] U. G. Poschinger, G. Huber, F. Ziesel, M. Deiss, M. Hettrich, S. A. Schulz, G. Poulsen, M. Drewsen, R. J. Hendricks, K. Singer, and F. Schmidt-Kaler, J. Phys. B: At. Mol. Opt. Phys. **42**, 154013 (2009).
 - [29] D. Leibfried, R. Blatt, C. Monroe, and D. Wineland, Rev. Mod. Phys. **75**, 281 (2003).
 - [30] See Supplemental Material at [URL will be inserted by publisher] for a detailed error discussion.
 - [31] K. Singer, U. G. Poschinger, M. Murphy, P. A. Ivanov, F. Ziesel, T. Calarco, and F. Schmidt-Kaler, Review of Modern Physics **82**, 2609 (2010).
 - [32] H. A. Füst, M. H. Goerz, U. G. Poschinger, M. Murphy, S. Montangero, T. Calarco, F. Schmidt-Kaler, K. Singer, and C. P. Koch, New Journal of Physics **16**, 075007 (2014).
 - [33] M. Palmero, S. Martinez-Garaot, U. G. Poschinger, A. Ruschhaupt, and J. G. Muga, New Journal of Physics **17**, 093031 (2015).